

# Prediction of Recurrence Patterns in Glioblastoma Using DSC-MRI Radiomics-Based Deep Learning

**Ka Young Shim**

Seoul National University College of Medicine

**Sung Won Chung**

Seoul National University College of Medicine

**Jae Hak Jeong**

Seoul National University College of Medicine

**Inpyeong Hwang**

Seoul National University Hospital

**Chul-Kee Park**

Seoul National University Hospital

**Tae Min Kim**

Seoul National University Hospital

**Sung-Hye Park**

Seoul National University Hospital

**Jae Kyung Won**

Seoul National University Hospital

**Joo Ho Lee**

Seoul National University Hospital

**Soon-Tae Lee**

Seoul National University Hospital

**Roh-Eul Yoo**

Seoul National University Hospital

**Koung Mi Kang**

Seoul National University Hospital

**Tae Jin Yun**

Seoul National University Hospital

**Ji-Hoon Kim**

Seoul National University Hospital

**Chul-Ho Sohn**

Seoul National University Hospital

**Kyu Sung Choi**

Seoul National University Hospital

**Seung Hong Choi** (✉ [verocay@snuh.org](mailto:verocay@snuh.org))

Seoul National University Hospital

**Keywords:** Glioblastoma, Deep Learning, Perfusion Weighted MRI

**Posted Date:** December 15th, 2020

**DOI:** <https://doi.org/10.21203/rs.3.rs-125593/v1>

**License:**   This work is licensed under a Creative Commons Attribution 4.0 International License. [Read Full License](#)

---

# Abstract

Glioblastoma remains the most devastating brain tumor despite optimal treatment, because of the high rate of recurrence. Distant recurrence has distinct genomic alterations compared to local recurrence, which requires different treatment planning both in clinical practice and trials. To date, perfusion-weighted MRI has revealed that perfusional characteristics of tumor are associated with prognosis. However, not much research has focused on recurrence patterns in glioblastoma: namely, local and distant recurrence. Here, we propose two different neural network models to predict the recurrence patterns in glioblastoma that utilizes high-dimensional radiomic profiles based on perfusion MRI: area under the curve (AUC) (95% confidence interval), 0.969 (0.903-1.000) for local recurrence; 0.864 (0.726-0.976) for distant recurrence for each patient in the validation set. This creates an opportunity to provide personalized medicine in contrast to studies investigating only group differences. Moreover, interpretable deep learning identified that salient radiomic features for each recurrence pattern are related to perfusional intratumoral heterogeneity. We also demonstrated that the combined salient radiomic features, or “radiomic risk score”, increased risk of recurrence/progression (hazard ratio, 1.61;  $p=0.03$ ) in multivariate Cox regression on progression-free survival.

## Introduction

Glioblastoma (GBM) remains the most aggressive primary brain tumor, with a median survival of 12–15 months despite optimal treatment<sup>1</sup>. The poor prognosis is due to the high rate of recurrence/progression<sup>2</sup>. In regions of physically disrupted blood brain barrier (BBB) by tumor cells, the contrast agents diffuse out of the vessels, manifesting enhancing lesions on contrast-enhanced T1-weighted images (CE T1WI) in nearly all GBM. These enhancing lesions are associated with dense tumor cells, and are the target for surgical resection<sup>3</sup>. However, CE T1WI is insufficient to distinguish paucicellular involvement of tumor from peritumoral edema, which is well-demonstrated on T2-weighted images (T2WI). T2 hyperintense area surrounding enhancing lesions on CE T1WI, should be considered as brain parenchyma infiltrated by isolated tumor cells, and radiation field should cover the area when planning radiation treatment<sup>4</sup>.

GBMs have high intratumoral heterogeneity (ITH), and result in inevitable recurrence<sup>5</sup>. Thus, many attempts have been made to predict relapse, or progression, and the prognosis of a tumor. Radiomics that extracts quantitative features from radiographic images is the latest approach, and many studies have been conducted to relate radiomic profiles to GBM's molecular subtypes, genetic mutations, and/or survivals<sup>6–8</sup>. Among them, radiomic features obtained from cerebral blood volume (CBV) maps, or hemodynamic parameter maps derived from dynamic susceptibility contrast-enhanced MRI (DSC MRI), have been reported as potential biomarkers to predict the prognosis of GBM<sup>9</sup>.

Recent surgical advances has increased rate of complete resection (CR) of contrast-enhancing lesions with the help of 5-aminolevulinic acid (5-ALA) guided resection, and intraoperative neurophysiologic monitoring, which leads to improved outcome<sup>10</sup>. However, GBM recurrence/progression is still almost inevitable, and further investigation for effective treatment strategy is highly required for recurrent GBM<sup>11</sup>. Distant recurrence (DR) has been known to have different tumor biology from local recurrence (LR), which represents low rate of retention of initial tumor mutations<sup>12</sup>, and thus requires different treatment strategy compared to LR. However, not much study has focused on the recurrence patterns in GBM. Moreover, no study has focused on the prediction of recurrence patterns after maximal surgical resection, especially at an individual level.

Here, we developed and validated the prediction model for recurrence patterns in GBM based on perfusion radiomics. We also identified salient radiomic features obtained from CBV maps to predict the recurrence patterns using interpretable deep learning, and analyzed whether the salient features are associated with prognosis. This creates an opportunity to provide personalized medicine, leading to optimal management in patients with glioblastoma.

## Results

### Patient characteristics

Under the inclusion and exclusion criteria, total 192 patients were finally included in our study (Fig. 1). The clinical characteristics of the GBM patients in the disease recurrence ( $n = 125$ ) and the non-recurrence ( $n = 67$ ) group are summarized in Table 1. There were no differences between the two groups in regards of the age, and radiation dose. The male patients were more in the recurrence group than in non-recurrence group (86 of 125 vs 29 of 67, respectively,  $p < 0.001$ ). O6-Methylguanine-DNA methyltransferase (MGMT) promotor methylation was more frequently observed in the non-recurrence group than in recurrence group (44 of 67 vs 50 of 125, respectively,  $p < 0.001$ ). Isocitrate dehydrogenase (IDH) wildtype was more frequent in the recurrence group than the non-recurrence group (121 of 125 vs 57 of 67, respectively,  $p = 0.01$ ). The mean duration of LR and DR were  $416 \pm 298$  (range, 22 - 1,666) and  $342 \pm 189$  (range, 22 - 1,042) days respectively, which resulted in no statistical significance ( $p = 0.051$ ).

Table 1  
Clinical characteristics of the study population

| Characteristics          | Total<br>( $n = 192$ ) | Recurrence<br>( $n = 125$ ) | Non-recurrence ( $n = 67$ ) | $p$ -value        |  |
|--------------------------|------------------------|-----------------------------|-----------------------------|-------------------|--|
| Mean age (years)         | 60.2                   | $60.8 \pm 13.5$             | $59.1 \pm 12.8$             | 0.37*             |  |
| Mean radiation dose (Gy) | 56.6                   | $56.3 \pm 7.7$              | $57.2 \pm 7.0$              | 0.42*             |  |
| Sex                      |                        |                             |                             | $< 0.001^\dagger$ |  |
|                          | Female                 | 115                         | 86                          | 29                |  |
|                          | Male                   | 77                          | 39                          | 38                |  |
| Methylated MGMT promoter |                        |                             |                             | $< 0.001^\dagger$ |  |
|                          | Positive               | 94                          | 50                          | 44                |  |
|                          | Negative               | 98                          | 75                          | 23                |  |
| IDH1/2 mutation          |                        |                             |                             | 0.01 <sup>†</sup> |  |
|                          | Positive               | 14                          | 4                           | 10                |  |
|                          | Negative               | 178                         | 121                         | 57                |  |

### Image analysis

For perfusion radiomics, cerebral blood volume (CBV) maps were generated from DSC MRI. For each patient, total 1,702 radiomic features were obtained from two regions of interest (ROI) on both contrast-enhanced lesion, and non-

enhancing T2 hyperintense lesion of tumor, overlaid on the CBV map. The overall workflow from image process to analysis is given in Fig. 2, and the obtained radiomic profile of recurrent glioblastoma patients ( $n = 125$ ) is given in Supplementary Fig. 1.

## Performance and interpretation of prediction models for recurrence patterns

The sensitivity, specificity, accuracy, and area under the curve (AUC) of the prediction model for 1) LR vs non-LR was for 94.59%, 100.00%, 97.30%, and 0.995 (0.993–0.996) for discovery set, and 94.44%, 83.33%, 91.67%, and 0.969 (0.903-1.000) for validation set; and 2) DR vs non-DR was for 93.33%, 100.00%, 96.67%, and 0.986 (0.982–0.990) for discovery set, and 93.33%, 80.00%, 88.00%, and 0.864 (0.726–0.976) for validation set, respectively (Table 2).

Receiver operating characteristic (ROC) curves for validation set, and training curves for loss and accuracy of each model, are given in Supplementary Fig. 2. In 5-fold cross validation, mean AUC was  $0.82 \pm 0.09$  for LR; and  $0.86 \pm 0.05$  for DR (Fig. 3).

Table 2

Diagnostic performance of the prediction model for each recurrence pattern: discovery and validation set

|  | Discovery set   |                 |              |                     | Validation set  |                 |              |                     |
|--|-----------------|-----------------|--------------|---------------------|-----------------|-----------------|--------------|---------------------|
|  | Sensitivity (%) | Specificity (%) | Accuracy (%) | AUC (95% CI)        | Sensitivity (%) | Specificity (%) | Accuracy (%) | AUC (95% CI)        |
| Local recurrence                                   | 94.59           | 100.00          | 97.30        | 0.995 (0.993–0.996) | 94.44           | 83.33           | 91.67        | 0.969 (0.903–1.000) |
| Distant recurrence                                 | 93.33           | 100.00          | 96.67        | 0.986 (0.982–0.990) | 93.33           | 80.00           | 88.00        | 0.864 (0.726–0.976) |
| Abbreviations:                                     |                 |                 |              |                     |                 |                 |              |                     |
| AUC, area under the curve; CI, confidence interval |                 |                 |              |                     |                 |                 |              |                     |

For each model, force plots, decision plots, and summary plots<sup>13</sup> (detailed in Supplementary material), were obtained from Shapley additive explanations (SHAP) (given in Supplementary Fig. 3), and top 10 important features with largest feature importance values are listed in the Table 3. The representative cases with LR and DR are given in Fig. 4.

Table 3  
Top 10 important features of neural network models to predict each recurrence pattern

| Recurrence pattern                               | Feature names <sup>†</sup>                        | Importance values |
|--|---|-------------------|
| Local recurrence<br>(LR<br>vs<br>non-LR group)   | sub_wavelet_LLL_firstorder_10Percentile           | 14.48             |
|  | sub_wavelet_LLL_firstorder_Kurtosis*              | 9.00              |
|  | sub_original_shape_LeastAxisLength                | 7.38              |
|  | T1_wavelet_LHH_glcm_ClusterShade                  | 7.18              |
|  | sub_original_glszm_LowGrayLevelZoneEmphasis       | 6.71              |
|  | T1_wavelet_HLL_glcm_Idn                           | 6.19              |
|  | T1_wavelet_LHH_glcm_MCC*                          | 6.06              |
|  | sub_original_glcm_InverseVariance                 | 5.35              |
|  | sub_wavelet_HLH_glszm_SizeZoneNonUniformityNor... | 4.74              |
|  | T1_wavelet_HHL_firstorder_InterquartileRange      | 4.70              |
| Distant recurrence<br>(DR<br>vs<br>non-DR group) | T1_wavelet_HHH_gldm_DependenceNonUniformity*      | 5.99              |
|  | sub_wavelet_LHH_firstorder_Kurtosis               | 3.65              |
|  | sub_wavelet_HHH_firstorder_Energy                 | 3.43              |
|  | T1_wavelet_HLH_firstorder_Maximum                 | 3.09              |
|  | sub_wavelet_HLH_firstorder_Skewness               | 3.02              |
|  | sub_wavelet_HLL_glcm_ClusterShade                 | 2.09              |
|  | T1_original_glszm_SmallAreaLowGrayLevelEmphasis   | 1.95              |
|  | T1_original_shape_Elongation                      | 1.78              |
|  | sub_wavelet_LLH_glcm_Correlation                  | 1.48              |
| sub_wavelet_LHH_glcm_InverseVariance             | 1.39  |                   |

## Radiomic risk score

Using Cox regression with least absolute shrinkage and selection operator (Cox-LASSO), 3 features with non-zero coefficients were selected from total 64 features (i.e. 32 features obtained from each of two different prediction model). Next, a radiomic risk score was developed using a linear combination of the 3 selected features with coefficients obtained from Cox-LASSO (Eq. 1), and each patient was stratified into either a high- or low- “radiomic risk group” using the median values of radiomic risk scores for cut-offs<sup>14</sup>.

### Radiomic risk score

$$\begin{aligned} &= t1\_wavelet\_LHH\_glcm\_MCC \times 0.219 \\ &+ t1\_wavelet\_HHH\_gldm\_DependenceNonUniformity \times 0.121 \\ &+ sub\_wavelet\_LLL\_firstorder\_Kurtosis \times 0.068 \quad (\text{eq. 1}) \end{aligned}$$

In log-rank test, risk of recurrence was stratified between high and low radiomic risk group ( $p = 0.0047$ ) (Kaplan-Meier plots illustrated in Fig. 5a).

## Multivariate Cox proportional hazard model to predict progression free survival

In multivariate Cox regression model to predict progression free survival (PFS), among clinical and radiomic variables, MGMT status, and radiomic risk group were significant, and concordance index (C-index) was 0.66 (standard deviation = 0.03). More specifically, radiomic risk group experienced significantly shorter progression (i.e. hazard ratio (HR) = 1.61; 95% confidence interval (CI), 1.03–2.52;  $p = 0.035$ ). MGMT-methylation group experienced significantly longer progression (i.e. HR = 0.36; 95% CI, 0.25–0.54;  $p = 6.38 \times 10^{-7}$ ). However, IDH-mutation was not significant in the multivariate Cox model (HR = 0.46; 95% CI, 0.16–1.32;  $p = 0.147$ ), but significant when MGMT was excepted (HR = 0.26; 95% CI, 0.092–0.74;  $p = 0.011$ ) (Supplementary Fig. 4a) as well as in log-rank test ( $p = 0.0049$ ). Male sex (HR = 1.11; 95% CI, 0.75–1.63;  $p = 0.602$ ), and aged (HR = 1.00; 95% CI, 0.98–1.01;  $p = 0.858$ ) were not significant variables. Kaplan-Meier plots for each variable are illustrated in Figs. 5a-c. A forest plot, showing variables and HR with CI and  $p$ -values of multivariate Cox-regression model, is given in the Fig. 5d.

## Discussion

The utility of CBV in the prediction of GBM patient outcome has been demonstrated in several previous studies. Other studies have similarly showed that CBV features, associated with tumor aggressiveness, is valuable parameters for prediction of glioma patient survival and prognosis<sup>15,16</sup>. However, these studies have limited implication for precision medicine in that they focused to analyze whether the group difference exists or not. In contrast, deep learning has enabled accurate prediction at an individual level<sup>8</sup>. Moreover, the individual prediction of the recurrence patterns in GBM is crucial for optimal management of the affected patients<sup>17</sup>. In our study, we evaluated radiomic features from CBV maps to see whether the recurrence patterns in GBM patients, and prognosis could be predicted with these features, using deep learning and Cox-regression, respectively. Specifically, 32 useful radiomic features were selected among 1,702 features, and the recurrence pattern of each patient in validation set was predicted using multilayer perceptron network as a classifier, showing excellent performance. Subsequently, “radiomic risk score” was developed using the 3 selected features from the 64 combined radiomic features, which were obtained to predict recurrence patterns, and the score was an independent risk factor of progression in multivariate Cox regression. As a result, the radiomic features of the CBV maps based on non-enhancing T2 hyperintense lesions, and contrast-enhanced tumor, were most helpful for the prediction of the local recurrence and distant recurrence, respectively. Moreover, the PFS could largely be predicted by using the radiomic features of the CBV maps combined with clinical variables.

The accuracy and AUC of the LR prediction model were 97.30% and 0.995 (95% CI, 0.993-0.996) for discovery set; and 91.67% and 0.969 (95% CI, 0.903-1.000) for validation set, respectively. In the LR prediction, top three first-order,

and shape features extracted from non-enhancing T2 hyperintense lesions, *sub\_wavelet\_LLL\_firstorder\_10Percentile*, *sub\_wavelet\_LLL\_firstorder\_Kurtosis*, and *sub\_original\_shape\_LeastAxisLength*, showed the highest feature importance values using SHAP<sup>13</sup>, an extendable algorithm for interpretation of neural network models (Table 3): the first two features describe that tumors with higher CBV values (i.e. high *10Percentile*), peaked at higher levels than mean in the histogram of voxel intensity of non-enhancing T2 hyperintense lesions (i.e. high *Kurtosis*), which reflects higher infiltrating tumor cells in non-enhancing lesions, are associated with LR; and also non-enhancing lesions involving all directions equally (i.e. high *LeastAxisLength*), surrounding enhancing tumor, are associated with LR, which are consistent with previous studies<sup>18,19</sup>. In summary, high CBV values of nonenhancing T2 hyperintense lesions seemed to be the most useful parameter for LR prediction. Kim et al. also reported that CBV features from nonenhancing regions were useful for anticipating local recurrence, and even more significant if combined with fractional anisotropy<sup>20</sup>. Our LR prediction model results determined that in the CBV maps, nonenhancing area were more competent than contrast-enhanced regions.

The accuracy and AUC of the DR prediction model were 96.67% and 0.986 (95% CI, 0.982-0.990) for discovery set; and 88.00% and 0.864 (95% CI, 0.726-0.976) for validation set, respectively. The most important feature of the prediction model for DR was CE T1WI based textural features from CBV maps:

*T1\_wavelet\_HHH\_gldm\_DependenceNonUniformity* (Table 3). This parameter measures the similarity of dependence through the image, with a higher value indicating more heterogeneity, which reflects ITH of CBV maps in contrast-enhanced regions. Meanwhile, for both DR, and LR prediction, top important features were mostly wavelet features (Table 3). As the wavelet transform is very useful in texture analysis because of the linearity and the possibility of time/space localizations<sup>21</sup>, recurrence patterns could largely be predicted by textural radiomic features from CBV maps. In addition, texture analysis has proven to be an effective way to measure ITH, as shown in breast cancer, lung cancer, colorectal cancer, etc.<sup>22-24</sup>. In addition, contrast-enhanced areas on CE T1WI could reflect ITH<sup>25</sup>: GBM cells release BBB disrupting factors which are up-regulated with increased malignancy, thus enhancing endothelial cell permeability<sup>25</sup>. Thus, higher signal on CE T1WI implies relatively more compromised BBB in tissue that later recurred, also consistent with infiltrating tumor characteristics<sup>26</sup>.

DR has the apparent negative impact on survival of patients with malignant gliomas<sup>27</sup>. In addition, the nature of migratory glioma cells is highly associated with matrix adhesion which is mediated by signal transduction cascades used in transmembrane receptors<sup>28</sup>. Various genetic mutations to contributing DR in patients with GBM have been discovered including tumor suppressor gene *PTEN*, gene signaling to block apoptosis *SPOCK1*, *ANXA11*, and so forth<sup>29</sup>. As a result, DR of GBM is greatly related to highly malignant portions of GBM tumor cells which are well demonstrated in texture features from CBV map based on CE T1WI. In summary, because of DR's aggressive nature, the feature from contrast-enhanced areas was more important than features from non-enhancing T2 hyperintense lesions in the prediction model for DR, in contrast to LR.

Rapp et al. has reported that recurrence patterns affect the survival in GBM patients<sup>17</sup>. Similarly, in the present study, the radiomic risk variable, or the weighted combination of three selected radiomic features (Eq. 1) to predict the recurrence patterns, could predict the PFS using Cox regression model (C-index, 0.66), when combined with clinical variables: the radiomic risk variable increased the risk (HR=2.05,  $p = 0.0007$ ), and MGMT methylation decreased the risk of the recurrence (HR = 0.42,  $p = 2.95 \times 10^{-6}$ ), which is consistent with the previous study<sup>30</sup>. However, IDH mutation status was not significant ( $p=0.19$ ). Three selected features for radiomic risk variable were *T1\_wavelet\_LHH\_glcm\_MCC*, *T1\_wavelet\_HHH\_gldm\_DependenceNonUniformity*, and *sub\_wavelet\_LLL\_firstorder\_Kurtosis*. The result that the two features from contrast-enhanced areas is crucial for

predicting PFS, was consistent with previous studies that contrast enhancement is strongly associated with poor prognosis<sup>31</sup>. In addition, the two features were texture features regarding *glcm\_MCC*, and *gldm\_DependenceNonUniformity*, where maximal correlation coefficient (MCC) is a measure of complexity of the texture<sup>32</sup>. Both *MCC* and *DependenceNonUniformity* are also associated with variability of intensity values in contrast-enhanced lesions, which is consistent with that ITH is primarily related with the PFS.

Our study has several limitations. First, due to the retrospective design with relatively small sample size and single-centered data, the generalizability may be limited. Though we reduced the overfitting due to high-dimensionality by using dimension reduction, and data augmentation, the prediction model should be further improved using a larger dataset. In addition, radiomics data may be dependent on MR scanner or sequence settings, which was equalized in this study<sup>20</sup>. Further research with multicentered larger sample size with prospective design should be conducted to validate the generalizability of the developed model. Second, the recurrence is ultimately time-dependent data, however, we specified the recurrence “at one year” to treat them as binary outcome to simplify the prediction model. Further improvement can be made integrating time information such as time-to-progression to develop the prediction model. Third, multimodal MRI images were not utilized, and further improvement warrants the potential increase of the model performance. Lastly, to date, biological meaning of radiomics features is not fully understood. Thus, further researches for determining relationships among radiomics data and tumor biology are needed.

In conclusion, the radiomic features from CBV maps based on contrast-enhanced area and non-enhancing T2 hyperintense area were mainly important for predicting DR and LR, respectively. The CBV heterogeneity was a salient parameter for both recurrence patterns as well as survival: LR, DR, and PFS. By using relevant features to predict the recurrence patterns, PFS could largely be regressed/explained in GBM patients using Cox-regression model. Our results might be helpful for the optimal treatment planning as well as clinical trial designs in GBM, avoiding suboptimal patient selection.

## Methods

### *Patients*

This retrospective study was approved by the Institutional Review Board of Seoul National University Hospital. The Institutional Review Board waived the requirement for informed consent. The study protocol is performed in accordance with the relevant guidelines and regulations. Two hundred and ninety-five consecutive patients ( $n=295$ ) diagnosed with glioblastoma from April 2010 to September 2019 at Seoul National University Hospital from the radiology report database were enrolled to the study. The followings were the inclusion criteria: patients (a) had a histopathologic diagnosis of GBM for the first time based on the 2016 WHO classification of central nervous system tumors, (b) had preoperative (24–48 hours before the operation) and follow-up 3T MR imaging including contrast enhanced (CE) T1WI, DSC MRI and FLAIR, (c) underwent the standard treatment, concomitant chemoradiotherapy with temozolomide and six cycles of adjuvant temozolomide after maximal (gross-total and near-total; > 95% by volume) surgical resection of contrast-enhanced region, and (d) had follow-up period of  $\geq$  one year after surgery. The exclusion criteria were as follows: (a) sub-total resection (< 95% by volume) or biopsy ( $n=68$ ), (b) inadequate image quality for analysis ( $n=10$ ), and (c) follow up loss ( $n=25$ ). Under these inclusion and exclusion criteria, total 192 patients were finally included in our study (Figure 1). We specified the extent of resection as maximal resection at least (i.e. including complete resection), because we focused to investigate the recurrence pattern when no measurable residual enhancing lesions were left after surgery, excluding the recurrence from measurable residual tumor<sup>33,34</sup>.

All patients routinely visited the outpatient clinic and underwent follow-up brain MR imaging with a brain tumor evaluation protocol at our institution every 3 months for the first 2 years. Then the follow-up period was extended to 6 months if the patient had no evidence of progression, clinically or radiologically. Based on the Response Assessment in Neuro-Oncology (RANO) criteria, the neuro-oncology team of our institution, consisting of radiologists, neurosurgeons, neurooncologists, and radiation oncologists, assessed the progression, and according to the assessment, the patients were classified into disease recurrence and non-recurrence groups. Patients corresponding to any of the followings were considered to have disease recurrence over a 1-year follow-up after the completion of adjuvant TMZ<sup>35,36</sup>: (a) a greater than 25 % increase in the sum of the products of the perpendicular diameters of the enhancing lesions with the smallest tumor measurement, (b) any new lesion, (c) clear clinical deterioration not attributable to causes other than the tumor and (d) clear recurrence of non-measurable disease. The rest of the patients, who are not corresponding to all of the above, were grouped into non-recurrence group. As a result, our study population was categorized into disease recurrence group ( $n=125$ ), and non-recurrence group ( $n=67$ ). The progression free survival (PFS) was defined as the interval between the initial diagnosis by MRI examination and the assessment of disease progression, or the last follow-up if the patient had no evidence of disease in the last follow-up<sup>33</sup>.

Disease recurrence was identified in three types<sup>17</sup>: local recurrence ( $n=49$ ), distant recurrence ( $n=32$ ), and combined recurrence ( $n=44$ ) according to the following criteria. Local recurrence (LR) was defined radiologically as tumor regrowth around the resection cavity, which was considered as non-enhancing T2 hyperintense area after surgery. We defined both subependymal and leptomeningeal seeding as distant recurrence (DR)<sup>37</sup>, because GBM can spread through the CSF along the ventricles, leading to subependymal or ependymal enhancement on MRI. In our study, imaging criteria for subependymal seeding was linear or nodular enhancement of the subependymal region that was remote from the ventricular margin of the primary neoplasm. Leptomeningeal seeding was defined radiologically as linear or nodular enhancement in the subarachnoid space or along the pial surfaces of the brain or spinal cord<sup>38</sup>. While leptomeningeal seeding occurs in 4% of patients with glioma and is thought to be rare, subependymal seeding is associated with higher rate of recurrence of gliomas and the region has long been considered a common site for tumor invasion<sup>39,40</sup>. In addition, despite their seemingly different definition and incidence, Anderson et al.<sup>37</sup> revealed that subependymal and leptomeningeal seeding have equivalent clinical behavior regarding time to development of the disease, survival time from the diagnosis, rates of hydrocephalus and ventriculoperitoneal shunt placement, etc. Finally, to further analyze features specific to local, and distant recurrence, total enrolled patients ( $n=192$ ) were grouped into LR ( $n=93$ ) and non-LR ( $n=99$ ) group; and DR ( $n=76$ ) vs non-DR ( $n=116$ ) group (i.e. binary classification), respectively.

### ***Imaging protocol***

For tumor segmentation, the T1W 3D magnetization-prepared rapid acquisition gradient echo sequence before and after administration of gadobutrol (Gadovist; Bayer, Berlin, Germany; at a dose of 0.1 mmol/kg of body weight) and T2-FLAIR imaging were used for the enrolled patients. The DSC MRI protocols were acquired by using dedicated protocols in our institute. MR scan parameters are provided in Supplementary Table 1.

### ***Image Processing and Analysis***

The MR data including CE T1WI, FLAIR imaging and DSC MRI were transferred from the PACS workstation to a personal computer and processed with a software package (NordicICE v4.1.2; Nordic Neuro Lab, Bergen, Norway).

Prior to drawing regions of interest (ROIs), we performed coregistration of FLAIR and DCE MRI on postcontrast 3D T1WI as structural imaging, which was achieved automatically by an algorithm finding an optimal rigid transformation based on the geometric information<sup>41</sup>. Manual correction was followed for the best matching nonenhancing T2 highsignal-intensity lesions, if there was geometric distortion due to postsurgical changes. After the motion correction of DSC MRI, deconvolution with the arterial input function was performed in the pharmacokinetic model. Next, a cerebral blood volume (CBV) parametric map calculated from DSC MRI was generated on a pixel-by-pixel basis with leakage correction (detailed in Supplementary material). Subsequently, two ROIs were drawn slice by slice for tumor volume: (a) enhancing tumor (without necrotic regions) and (b) the non-enhancing T2 hyperintense lesions, which is illustrated in Supplementary Figure 5. The enhancing tumor areas were drawn semi-automatically on CE T1WI using seed growing and threshold segmentation (and manually, if we need). Then, enhancing tumor areas with necrosis were drawn by adding enhancing tumor and necrosis. Necrosis was defined as areas of relatively hypo-intense regions, frequently located within the enhancing tumoral regions, on CE T1WI<sup>42</sup>. The non-enhancing T2 hyperintense lesions were drawn by subtracting the enhancing tumor areas with necrosis from T2-FLAIR hyperintense lesions<sup>42</sup>. All the images were processed using NordiclCE (v4.1.2). ROIs were drawn by three well-trained medical students (J.H.J, K.Y.K and S.W.J) supervised by one expert radiologist (S.H.C., with 17 years of neuro-oncology imaging experience).

Next, the radiomic features from the information contained in the voxels of the segmented structure were extracted using NordiclCE. The radiomic features are composed of seven feature groups: 18 first-order features, 14 shape features (3D), 24 gray-level co-occurrence matrix (GLCM) features, 16 gray-level size zone matrix (GLSZM) features, 16 gray-level run-length matrix (GLRLM) features, 5 neighboring gray tone difference matrix (NGTDM) features, and 14 gray-level dependence matrix (GLDM) features. The full mathematical description and detailed number of each feature is in Supplementary material. The original features were radiomics features extracted from original images, resulting in 107 features in total.

Wavelet transformation was applied to the input image to extract intensity and textural features from different frequency bands and to obtain fused texture characteristics from two imaging modalities. As a result, each MRI sequence input produced a total of eight wavelet decomposition images as HHH, HLH, HHL, HLL, LHH, LLH, LHL, and LLL images, where 'H' stands for a high-pass filter and 'L' for a low-pass filter<sup>32</sup>. The first-order features and gray-scale variation features (GLCM, GLRLM, GLSZM, NGTDM, GLDM features) were then applied to the wavelet-transformed images for 18 first-order features + 75 gray-scale variation features multiplied by eight images, thereby yielding 744 wavelet features. Finally, 851 radiomic features (107 original features, and 744 wavelet features) were respectively extracted from (a) enhancing lesions and (b) the non-enhancing T2 hyperintense lesions based on CBV maps, resulting in total 1,702 features from each patient. The overall workflow from image process to analysis is illustrated in Figure 2, and the radiomic profile of recurrent glioblastoma patients ( $n=125$ ) is given in the Supplementary Figure 1.

***Tissue diagnosis and genetic analysis are given in the Supplementary Material***

### ***Neural network model***

All 1,702 radiomic features were z-normalized. Since the radiomic data is a high-dimensional data, or large dimension of feature ( $d=1,702$ ) compared to the sample size ( $n=192$ ) for the model to be trained, feature selection was essential to avoid "curse of dimensionality". Recursive feature elimination with support vector machine (SVM-RFE)<sup>43</sup> was performed to select important features by repetitively removing subsets of features with small weights until 32 features were left. Using the selected features, we developed the two different neural network models to predict

recurrence patterns. Input features ( $d=32$ ), reduced dimension using SVM-RFE, were passed through 5 hidden layers to get the final output of prediction score for two different binary classification tasks: 1) LR vs non-LR, and 2) DR vs non-DR. Overall model architecture is illustrated in Supplementary Figure 6.

To augment the insufficient train/discovery dataset, as well as to deal with class imbalance, we used synthetic minority oversampling technique (SMOTE)<sup>44</sup>, which oversamples the minority class to match the number of samples in majority class, improving the model performance. We only augmented the train/discovery dataset, not validation set, because validation with synthetic data is not valid evaluation. The recurrence prediction model was developed on a randomly split 80% (train/discovery set), and validated on the remaining 20% of data (validation set). To evaluate the diagnostic performance of the model, sensitivity, specificity, and accuracy was obtained, and area under the curve (AUC) was also obtained using receiver operating characteristic (ROC) analysis. To report more generalized performance, 5-fold cross validation was also performed to obtain mean standard deviation of AUC.

To interpret and understand the features that the neural network model “thinks” are important, we used Shapley additive explanations (SHAP) for each model, which is an additive interpreting model for existing deep learning models<sup>13</sup>. All the implementation is detailed in Supplementary material.

### ***Statistical analysis***

Subsequent analysis was performed by using software R version 3.6.1 (R Foundation for Statistical Computing, Vienna, Austria). For all analyses, only  $p < 0.05$  was considered statistically significant. Clinical characteristics, including age, sex, date of surgery, radiation dose, date of recurrence, and genetic information, were recorded for each patient. Fisher’s exact test was performed for categorical data. The data for each parameter were assessed for normality with the Kolmogorov-Smirnov test. An unpaired Student’s t test was performed to compare data between the disease recurrence and non-recurrence groups. To examine whether the obtained features predicting recurrence patterns can also predict progression free survival (PFS), we developed a Cox proportional hazard model to regress the PFS with the total 64 selected features obtained above in the prediction model of LR vs non-LR, and DR vs non-DR (32 features for each, respectively). Among 64 features, Cox regression with least absolute shrinkage and selection operator (Cox-LASSO) was performed to select important features (i.e. features with non-zero weights above threshold after LASSO regularization). Next, a radiomic score was developed using a linear combination of the selected features with coefficients obtained from Cox-LASSO model (eq. 1), and each patient was stratified into either a high- or low- “radiomic risk group” using the median values of radiomic scores for cut-offs<sup>14</sup>. Finally, using 5 variables (i.e. 4 clinical variables: sex, age, MGMT methylation, IDH mutation; and radiomic risk group), a multivariate Cox regression model was developed, and concordance index (C-index) was also obtained to evaluate the performance of the Cox model. All the survival analysis was performed using “survival” R-package.

## **Declarations**

### **Data Availability**

All relevant data are available on request to correspondence. All codes for model implementation and analysis will soon to be uploaded at <https://github.com/kyuchoi>.

### **Acknowledgements**

We thank Yurim Kang, BS, and Seong Yeong Lee, BS, for their invaluable assistance with data collection and analysis.

## Author contributions

| Name            | Affiliation   | Contribution   |
|-----------------|---|--|
| Ka Young Shim   | Seoul National University College of Medicine   | Analyzed and interpreted the data; drafted the manuscript for intellectual content                     |
| Sung Won Chung  | Seoul National University College of Medicine   | Analyzed and interpreted the data; drafted the manuscript for intellectual content                     |
| Jae Hak Jeong   | Seoul National University College of Medicine   | Analyzed and interpreted the data; drafted the manuscript for intellectual content                     |
| Inpyeong Hwang  | Department of Radiology, Seoul National University Hospital   | Major role in the acquisition of data  |
| Chul-Kee Park   | Department of Neurosurgery and Biomedical Research Institute  | Major role in the acquisition of data  |
| Tae Min Kim     | Department of Internal Medicine and Cancer Research Institute, Seoul National University Hospital               | Major role in the acquisition of data  |
| Sung-Hye Park   | Department of Pathology, Seoul National University Hospital   | Major role in the acquisition of data  |
| Jae Kyung Won   | Department of Pathology, Seoul National University Hospital   | Major role in the acquisition of data  |
| Joo Ho Lee      | Department of Radiation Oncology and Cancer Research Institute, Seoul National University Hospital              | Major role in the acquisition of data  |
| Soon-Tae Lee    | Department of Neurology, Seoul National University Hospital   | Major role in the acquisition of data  |
| Roh-Eul Yoo     | Department of Radiology, Seoul National University Hospital   | Major role in the acquisition of data  |
| Koung Mi Kang   | Department of Radiology, Seoul National University Hospital   | Major role in the acquisition of data  |
| Tae Jin Yun     | Department of Radiology, Seoul National University Hospital   | Major role in the acquisition of data  |
| Ji-Hoon Kim     | Department of Radiology, Seoul National University Hospital   | Major role in the acquisition of data  |
| Chul-Ho Sohn    | Department of Radiology, Seoul National University Hospital   | Major role in the acquisition of data  |
| Kyu Sung Choi   | Graduate School of Medical Science and Engineering, Korea Advanced Institute for Science and Technology (KAIST) | Analyzed and interpreted the data; drafted the manuscript for intellectual content                     |
| Seung Hong Choi | Department of Radiology, Seoul National University Hospital   | Design and conceptualized study; interpreted the data; revised the manuscript for intellectual content |

## References

1. Wen, P. Y. & Kesari, S. Malignant gliomas in adults. *New England Journal of Medicine* **359**, 492–507 (2008).
2. Ekinici, G. *et al.* Early-postoperative magnetic resonance imaging in glial tumors: prediction of tumor regrowth and recurrence. *Eur J Radiol* **45**, 99–107, doi:10.1016/s0720-048x(02)00027-x (2003).
3. Sarkaria, J. N. *et al.* Is the blood-brain barrier really disrupted in all glioblastomas? A critical assessment of existing clinical data. *Neuro Oncol* **20**, 184–191, doi:10.1093/neuonc/nox175 (2018).
4. Watanabe, M., Tanaka, R. & Takeda, N. Magnetic resonance imaging and histopathology of cerebral gliomas. *Neuroradiology* **34**, 463–469, doi:10.1007/bf00598951 (1992).
5. Qazi, M. A. *et al.* Intratumoral heterogeneity: pathways to treatment resistance and relapse in human glioblastoma. *Ann Oncol* **28**, 1448–1456, doi:10.1093/annonc/mdx169 (2017).
6. McGarry, S. D. *et al.* Magnetic Resonance Imaging-Based Radiomic Profiles Predict Patient Prognosis in Newly Diagnosed Glioblastoma Before Therapy. *Tomography* **2**, 223–228, doi:10.18383/j.tom.2016.00250 (2016).
7. Aghi, M. *et al.* Magnetic resonance imaging characteristics predict epidermal growth factor receptor amplification status in glioblastoma. *Clin Cancer Res* **11**, 8600–8605, doi:10.1158/1078-0432.CCR-05-0713 (2005).
8. Choi, K. S., Choi, S. H. & Jeong, B. Prediction of IDH genotype in gliomas with dynamic susceptibility contrast perfusion MR imaging using an explainable recurrent neural network. *Neuro Oncol* **21**, 1197–1209 (2019).
9. Lee, J. *et al.* Texture Feature Ratios from Relative CBV Maps of Perfusion MRI Are Associated with Patient Survival in Glioblastoma. *AJNR Am J Neuroradiol* **37**, 37–43, doi:10.3174/ajnr.A4534 (2016).
10. Stummer, W. & Kamp, M. A. The importance of surgical resection in malignant glioma. *Current opinion in neurology* **22**, 645–649 (2009).
11. van Linde, M. E. *et al.* Treatment outcome of patients with recurrent glioblastoma multiforme: a retrospective multicenter analysis. *Journal of neuro-oncology* **135**, 183–192 (2017).
12. Kim, J. *et al.* Spatiotemporal evolution of the primary glioblastoma genome. *Cancer cell* **28**, 318–328 (2015).
13. Lundberg, S. M. & Lee, S.-I. in *Advances in neural information processing systems*. 4765–4774.
14. Liang, C. *et al.* The development and validation of a CT-based radiomics signature for the preoperative discrimination of stage I-II and stage III-IV colorectal cancer. *Oncotarget* **7**, 31401 (2016).
15. Boxerman, J. L., Schmainda, K. M. & Weisskoff, R. M. Relative cerebral blood volume maps corrected for contrast agent extravasation significantly correlate with glioma tumor grade, whereas uncorrected maps do not. *AJNR Am J Neuroradiol* **27**, 859–867 (2006).
16. Mackin, D. *et al.* Measuring Computed Tomography Scanner Variability of Radiomics Features. *Invest Radiol* **50**, 757–765, doi:10.1097/RLI.0000000000000180 (2015).
17. Rapp, M. *et al.* Recurrence pattern analysis of primary glioblastoma. *World neurosurgery* **103**, 733–740 (2017).
18. Kim, R. *et al.* Prognosis prediction of non-enhancing T2 high signal intensity lesions in glioblastoma patients after standard treatment: application of dynamic contrast-enhanced MR imaging. *Eur Radiol* **27**, 1176–1185 (2017).
19. Ruiz-Ontañón, P. *et al.* Cellular plasticity confers migratory and invasive advantages to a population of glioblastoma-initiating cells that infiltrate peritumoral tissue. *Stem cells* **31**, 1075–1085 (2013).
20. Kim, J. Y. *et al.* Radiomics in peritumoral non-enhancing regions: fractional anisotropy and cerebral blood volume improve prediction of local progression and overall survival in patients with glioblastoma. *Neuroradiology* **61**, 1261–1272, doi:10.1007/s00234-019-02255-4 (2019).

21. Materka, A. & Strzelecki, M. Texture analysis methods—a review. *Technical university of lodz, institute of electronics, COST B11 report, Brussels*, 9–11 (1998).
22. Kim, J.-H. *et al.* Breast Cancer Heterogeneity: MR Imaging Texture Analysis and Survival Outcomes. *Radiology* **282**, 665–675, doi:10.1148/radiol.2016160261 (2017).
23. Yoon, S. H. *et al.* Tumor Heterogeneity in Lung Cancer: Assessment with Dynamic Contrast-enhanced MR Imaging. *Radiology* **280**, 940–948, doi:10.1148/radiol.2016151367 (2016).
24. Ng, F., Kozarski, R., Ganeshan, B. & Goh, V. Assessment of tumor heterogeneity by CT texture analysis: can the largest cross-sectional area be used as an alternative to whole tumor analysis? *Eur J Radiol* **82**, 342–348, doi:10.1016/j.ejrad.2012.10.023 (2013).
25. Schneider, S. W. *et al.* Glioblastoma cells release factors that disrupt blood-brain barrier features. *Acta Neuropathol* **107**, 272–276, doi:10.1007/s00401-003-0810-2 (2004).
26. Hynes, R. O. Integrins: versatility, modulation, and signaling in cell adhesion. *Cell* **69**, 11–25, doi:10.1016/0092-8674(92)90115-s (1992).
27. Parsa, A. T. *et al.* Prognostic significance of intracranial dissemination of glioblastoma multiforme in adults. *J Neurosurg* **102**, 622–628, doi:10.3171/jns.2005.102.4.0622 (2005).
28. Giese, A., Bjerkvig, R., Berens, M. E. & Westphal, M. Cost of migration: invasion of malignant gliomas and implications for treatment. *J Clin Oncol* **21**, 1624–1636, doi:10.1200/JCO.2003.05.063 (2003).
29. Kato, H. *et al.* PTEN gene mutation and high MIB-1 labeling index may contribute to dissemination in patients with glioblastoma. *J Clin Neurosci* **11**, 37–41, doi:10.1016/j.jocn.2002.09.001 (2004).
30. Binabaj, M. M. *et al.* The prognostic value of MGMT promoter methylation in glioblastoma: A meta-analysis of clinical trials. *Journal of cellular physiology* **233**, 378–386 (2018).
31. Gutman, D. A. *et al.* MR imaging predictors of molecular profile and survival: multi-institutional study of the TCGA glioblastoma data set. *Radiology* **267**, 560–569, doi:10.1148/radiol.13120118 (2013).
32. Wang, J. Z. Wavelets and imaging informatics: A review of the literature. *Journal of Biomedical Informatics* **34**, 129–141 (2001).
33. Hwang, I. *et al.* Dynamic Contrast-Enhanced MR Imaging of Nonenhancing T2 High-Signal-Intensity Lesions in Baseline and Posttreatment Glioblastoma: Temporal Change and Prognostic Value. *American Journal of Neuroradiology* **41**, 49–56 (2020).
34. Kim, R. *et al.* Prognosis prediction of non-enhancing T2 high signal intensity lesions in glioblastoma patients after standard treatment: application of dynamic contrast-enhanced MR imaging. *Eur Radiol* **27**, 1176–1185, doi:10.1007/s00330-016-4464-6 (2017).
35. Wen, P. Y. *et al.* Updated response assessment criteria for high-grade gliomas: response assessment in neuro-oncology working group. *J Clin Oncol* **28**, 1963–1972, doi:10.1200/JCO.2009.26.3541 (2010).
36. Yoo, R.-E. *et al.* Dynamic contrast-enhanced MR imaging in predicting progression of enhancing lesions persisting after standard treatment in glioblastoma patients: a prospective study. *Eur Radiol* **27**, 3156–3166 (2017).
37. Andersen, B. M., Miranda, C., Hatzoglou, V., DeAngelis, L. M. & Miller, A. M. Leptomeningeal metastases in glioma: The Memorial Sloan Kettering Cancer Center experience. *Neurology* **92**, e2483-e2491 (2019).
38. Witham, T. F. *et al.* Survival of patients with high grade glioma treated with intrathecal thiotriethylenephosphoramidate for ependymal or leptomeningeal gliomatosis. *Cancer: Interdisciplinary International Journal of the American Cancer Society* **86**, 1347–1353 (1999).

39. Waqas, M., Iftikhar, M., Siddiqui, U. T. & Enam, S. A. Ependymal enhancement on magnetic resonance imaging for the identification of high-grade gliomas. *Surgical neurology international* **8** (2017).
40. Dardis, C., Milton, K., Ashby, L. & Shapiro, W. Leptomeningeal metastases in high-grade adult glioma: development, diagnosis, management, and outcomes in a series of 34 patients. *Frontiers in neurology* **5**, 220 (2014).
41. Pluim, J. P., Maintz, J. A. & Viergever, M. A. Mutual-information-based registration of medical images: a survey. *IEEE transactions on medical imaging* **22**, 986–1004 (2003).
42. Prasanna, P., Patel, J., Partovi, S., Madabhushi, A. & Tiwari, P. Radiomic features from the peritumoral brain parenchyma on treatment-naïve multi-parametric MR imaging predict long versus short-term survival in glioblastoma multiforme: Preliminary findings. *Eur Radiol* **27**, 4188–4197, doi:10.1007/s00330-016-4637-3 (2017).
43. Guyon, I., Weston, J., Barnhill, S. & Vapnik, V. Gene selection for cancer classification using support vector machines. *Machine learning* **46**, 389–422 (2002).
44. Chawla, N. V., Bowyer, K. W., Hall, L. O. & Kegelmeyer, W. P. SMOTE: synthetic minority over-sampling technique. *Journal of artificial intelligence research* **16**, 321–357 (2002).

## Figures

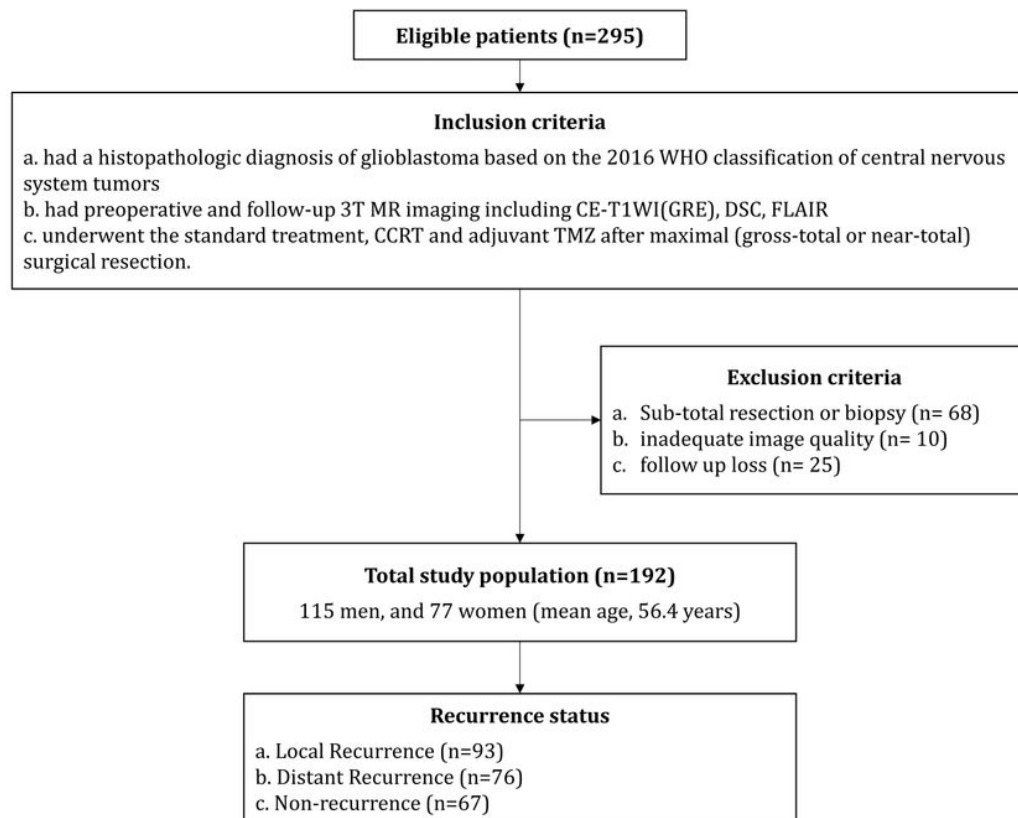


**Figure 1**

Patient inclusion/exclusion criteria

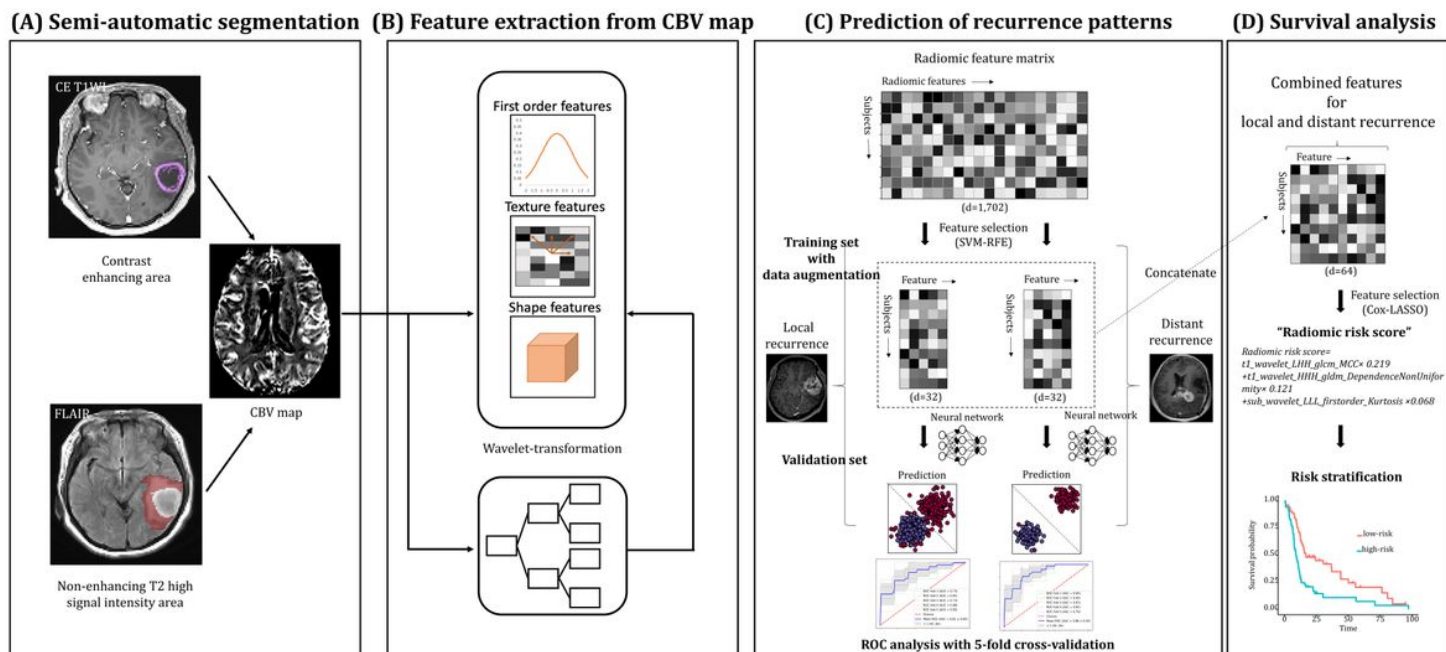


**Figure 2**

Overall workflow from tumor segmentation to prediction of recurrence patterns, and survival analysis. (A) Segmentation of contrast-enhanced and non-enhancing T2 hyperintense areas. (B) Multiple radiomic profiles including first-order, textural, shape and wavelet-transformed features were automatically calculated from contrast-enhanced and non-enhancing T2 hyperintense areas based on CBV map. Radiomic feature matrix (subjects × features) was obtained from image processing. (C) Two multilayer perceptron models were trained and validated to predict local and distant recurrence of glioblastoma, respectively. The prediction models were developed based on 32 features each, which were selected using SVM-RFE among 1,702 features of the radiomic feature matrix. (D) The three selected features from the 64 features in the multilayer perceptron models using Cox-LASSO were used to develop "radiomic risk score". The developed radiomic risk score was subjected to Cox proportional hazard model in addition to clinical variables to regress the progression free survival (PFS). Abbreviations: CBV, cerebral blood volume; SVM-RFE, recursive feature elimination with support vector machine; Cox-LASSO, Cox regression with least absolute shrinkage and selection operator.

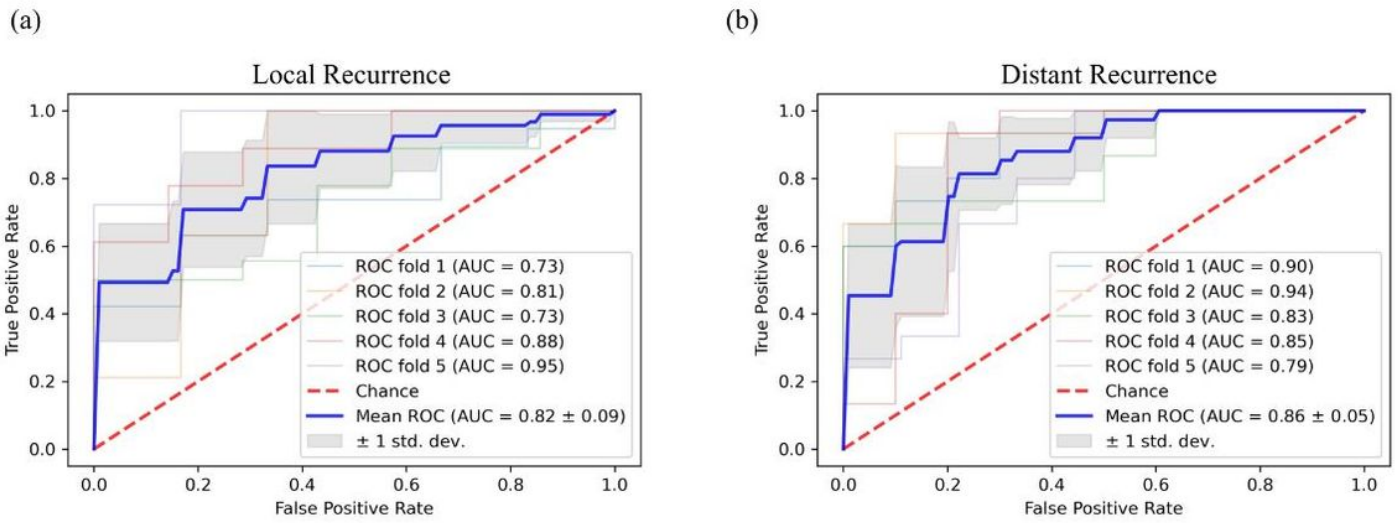
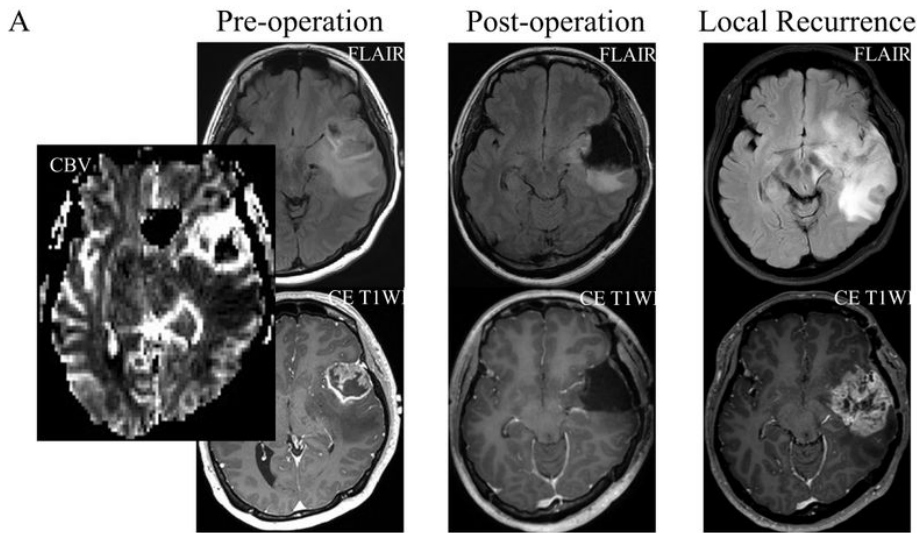
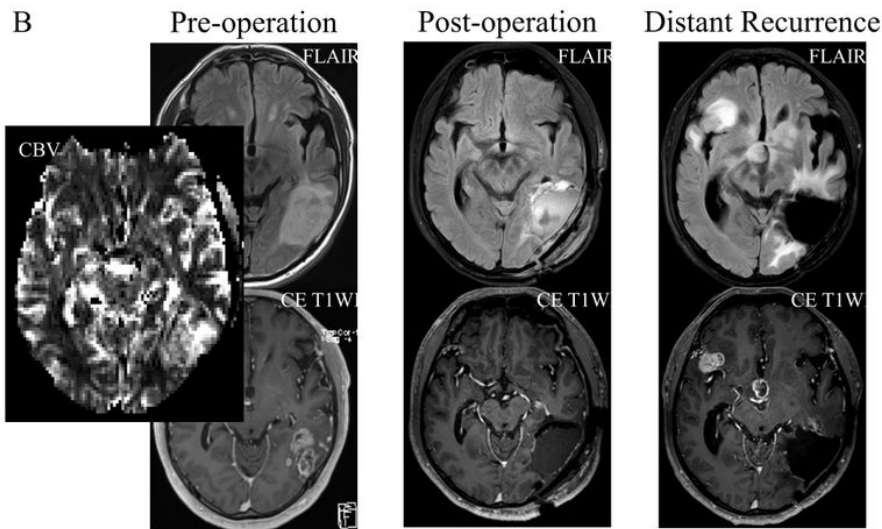


**Figure 3**

Receiver operating characteristics (ROC) curves of prediction models for recurrence patterns with 5-fold cross validation for (a) local recurrence, and (b) distant recurrence.



T1\_wavelet-LHH\_glm\_MCC: 0.72  
 T1\_wavelet-HHH\_gldm\_DependenceNonUniformity: 5.90  
 sub\_wavelet-LLL\_firstorder\_Kurtosis: 7.75



T1\_wavelet-LHH\_glm\_MCC: 0.69  
 T1\_wavelet-HHH\_gldm\_DependenceNonUniformity: 247.23  
 sub\_wavelet-LLL\_firstorder\_Kurtosis: 4.85

**Figure 4**

Representative glioblastoma cases with local recurrence (A) and with distant recurrence (B), respectively. (A) A glioblastoma patient who had early local recurrence (recurrence free survival = 12 months) after surgery. The contrast-enhanced glioblastoma with necrosis and high CBV was noted on pre-operative MRI, and total resection of the contrast-enhanced area was performed. In this patient, local recurrence was developed on follow-up MRI. (B) A glioblastoma patient who had early distant recurrence (recurrence free survival = 11 months) after surgery. The contrast-enhanced glioblastoma with necrosis and high CBV was noted on pre-operative MRI, and total resection of the contrast-enhanced area was performed. In this patient, distant recurrence was developed in the right sylvian fissure and suprasellar area. The distant recurrence case had a 42 times larger value of

T1\_wavelet\_HHH\_gldm\_DependenceNonUniformity of CBV map, which represents the non-uniformity of gray level values, and thus heterogeneity of tumor, compared with the local recurrence case.

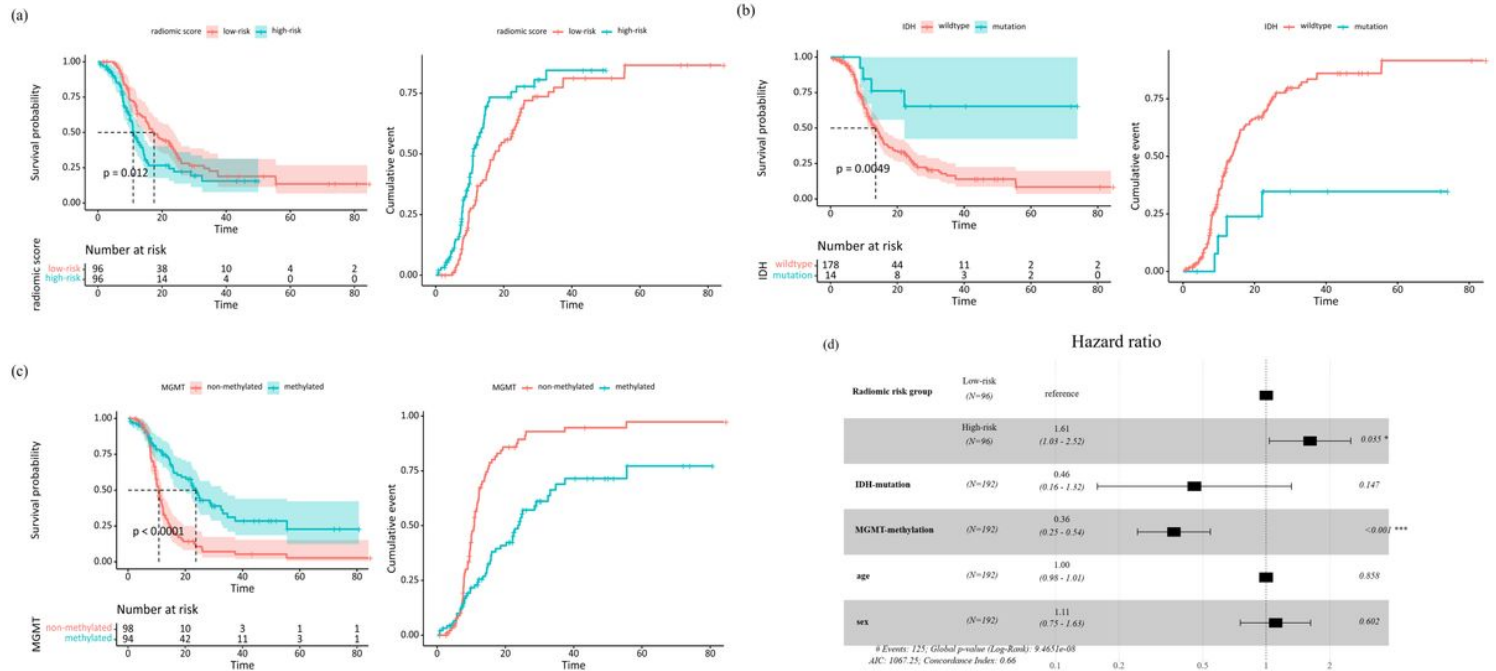


**Figure 5**

Kaplan-Meier survival curves showing progression free survival (PFS): risk of recurrence was stratified between (a) high and low radiomic risk group ( $p=0.0047$ ), (b) IDH-mutation and wildtype ( $p=0.0049$ ), and (c) MGMT-methylation and unmethylation ( $p<0.0001$ ). (d) Forest plot of multivariate Cox-regression model Note: p-values are obtained from the log-rank test which compares two survival functions according to risk group. 95% confidence intervals of survival functions are indicated as gray zone. Bottom tables indicate the actual number of patients at risk for the survival time according to the risk group.

## Supplementary Files

This is a list of supplementary files associated with this preprint. Click to download.

- [Supplementarymaterials.docx](#)